Elucidating the role of a molecular anion in mutual neutralisation reactions

Mathias Poline[1], Arnaud Dochain[2], MingChao Ji[1], Paul Martini[1], Stefan Rosén[1], Mikael Björkhage[1], Mikael Blom[1], Peter Reinhed[1], Ansgar Simonsson[1], Henrik Cederquist[1], Henning Zettergren[1], Henning T. Schmidt[1], Mats Larsson[1], Steve Ndengué[3], Ernesto Quintas-Sánchez[4], Richard Dawes[4], Shaun G. Ard[5], Nicholas S. Shuman[5], Albert A. Viggiano[5], Richard D. Thomas[1*]

[1]Department of Physics, Stockholm University, Stockholm, SE-10691, Sweden.
[2]Institute of Condensed Matter and Nanosciences, Université Catholique de Louvain, Louvain-la-Neuve, B-1348, Belgium.
[3]Department of Physics and Astronomy, Haverford College, Haverford, 19041, Pennsylvania, USA.
[4]Missouri University of Science and Technology, Rolla, 65409-0010, Missouri, USA.
[5]Space Vehicles Directorate, Air Force Research Laboratory, Kirtland AFB, Albuquerque, 87117, New Mexico, USA.

*Corresponding author(s). E-mail(s): rdt@fysik.su.se;

Supplementary Information

Supplementary text concerning: Data evaluation, two-body analysis, three-body analysis, three-body reaction dynamics, the free-rotor model in two-step reactions, potential energy surface calculations, wavepacket propagation dynamics, modelling flow-tube fluorescence.
Four new Figures: S1 to S4.
One new Table: S1.
Three new references: (51-53).

Here we present supporting information and analysis to the discussions in the main text. The first section discusses two- and three-body data analysis, the second section presents the calculations of the relevant excited states in NO_2; the third section discusses the flowing afterglow measurements to determine fluorescence rates and branching fractions.

1 Data evaluation

In order to evaluate the data, appropriate methods must be used to determine the momentum vectors and energies of the products. The reaction can lead to both two- and three-body products, and these are treated independently. Details are found in references [1, 4, 23, 24]

1.1 Two-body analysis

In MN of ground state $NO^+(X\ ^1\Sigma^+)$ with $NO_2^-(\tilde{X}\ ^1A_1)$ at a collision energy of $E_{c.m} = 0$ eV, the following two-body, non-dissociative product channels are available:

$$NO^+ + NO_2^- \rightarrow \quad NO(X) + NO_2(\tilde{X}) \quad \Delta H = -6.99\ \text{eV} \tag{S1a}$$

$$\rightarrow \quad NO(X) + NO_2(\tilde{A}) \quad \Delta H = -5.70\ \text{eV} \tag{S1b}$$

$$\rightarrow \quad NO(X) + NO_2(\tilde{B}) \quad \Delta H = -5.18\ \text{eV} \tag{S1c}$$

$$\rightarrow \quad NO(X) + NO_2(\tilde{C}) \quad \Delta H = -5.10\ \text{eV} \tag{S1d}$$

$$\rightarrow \quad NO(A) + NO_2(\tilde{X}) \quad \Delta H = -1.54\ \text{eV} \tag{S1e}$$

The reaction enthalpies quoted here assume that there is no ro-vibrational excitation in either of the parent ions or the neutral molecular products. Including the collision energy, $E_{c.m}$, and any internal energy in the parent ions will change this value. In a

two-body reaction, the calculation of the final kinetic energy and momentum vectors is straightforward, see, e.g. [1, 4]. The contribution from any three-body data must be subtracted from the two-body data to yield the correct distribution [1]. Figure S1, shows these two distributions, i.e., the measured two-body E_{K_f} data and the two-out-of-three-body E_{K_f} contribution, which was obtained by randomly selecting two events from the three-body data. This distribution was scaled to fit with the lower energy part of the spectrum, where MN typically does not contribute. The corrected distribution is shown in the main manuscript.

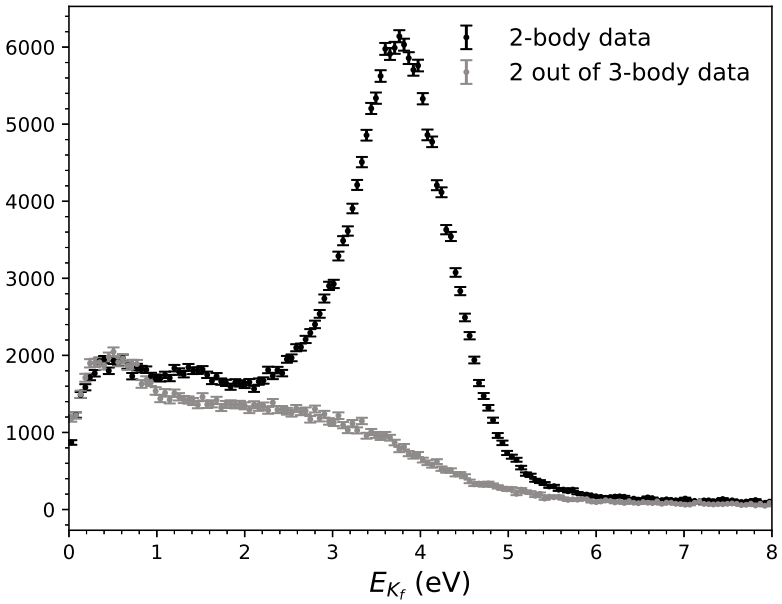

Fig. S1 MN of $NO^+ + NO_2^- \rightarrow NO + NO_2 + E_{K_f}$. Two-body and two-out-of-three-body E_{K_f} release distributions for the NO + NO_2 products.

This process also allows to retrieve the detection efficiency ϵ in the experiment. The probability to detect two products out of a three-body event, is given as $3\epsilon^2(1-\epsilon)$, while the probability to detect three is ϵ^3. From the ratio between the

number of three-body events and the number of two-out-of-three body events in the measured two-body distribution, we retrieve a detection efficiency of about 35%, which is slightly larger than what was obtained in a previous experiment ($\sim$ 30%) [2]. However, the detection efficiency of the detection system likely depends on the kinetic energies of the impacting neutrals; arrival time differences; the particular operating voltages of the microchannel plates and phosphor screen; the number of particles detected, with all aspects being different for the two experiments.

1.2 Three-body analysis

Under identical MN reaction conditions, the following three-body product channels are available:

$$\mathrm{NO^+ + NO_2^-} \rightarrow \quad \mathrm{N(^4S) + O(^3P) + NO_2(\tilde{X})} \quad \Delta H = -0.44\ \mathrm{eV} \tag{S2a}$$

$$\rightarrow \quad \mathrm{NO(X) + NO(X) + O(^3P)} \quad \Delta H = -3.82\ \mathrm{eV} \tag{S2b}$$

$$\rightarrow \quad \mathrm{NO(X) + NO(X) + O(^1D)} \quad \Delta H = -1.85\ \mathrm{eV} \tag{S2c}$$

The values quoted here are determined in a similar fashion to those earlier. There is insufficient available reaction energy to form $\mathrm{NO(A^2\Sigma^+)}$ in these reactions.

In order to identify the products, and yield the E_{K_f} distributions and corresponding Dalitz plot, the center-of-mass (R_{cm}) were computed for each possible permutation of the masses, for the two possible channels, N + O + NO_2 and NO + NO + O. Analysis shows that a much broader R_{cm} distribution is obtained assuming N + O + NO_2 dissociation, than assuming NO + NO + O break-up. This is shown in Figure S2, which plots the R_{cm} distributions in the x- (blue) and y- (red) directions, for the two different channels. It was thus concluded that the NO + NO + O is the

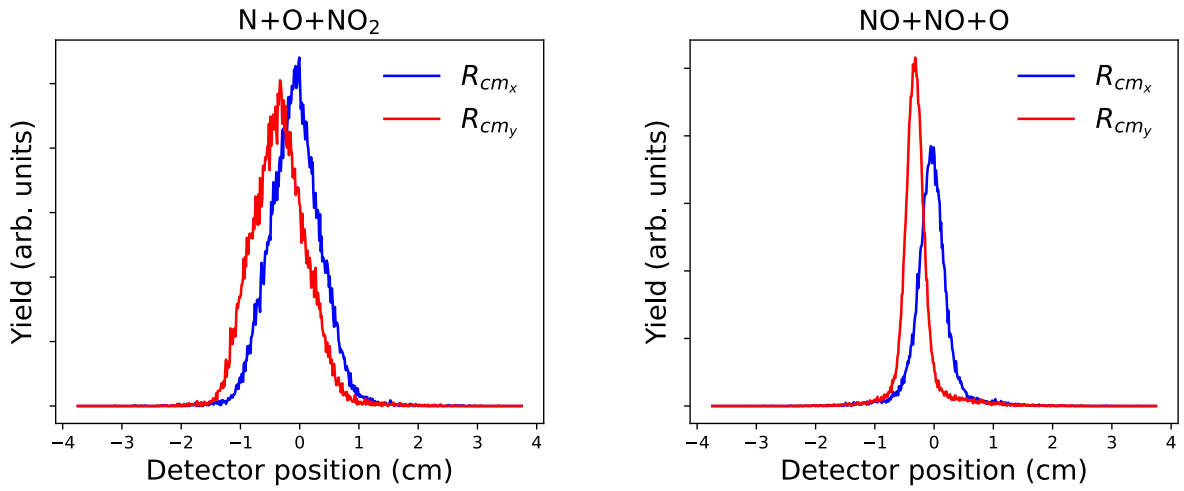

Fig. S2 Center-of-mass distributions in the x and y positions on the detector, $R_{cm_{x,y}}$, assuming (a) $NO^+ + NO_2^- \rightarrow N + O + NO_2$, (b) $NO^+ + NO_2^- \rightarrow NO + NO + O$

dominating channel. Furthermore the absence of any feature at the E_{K_f} value of channel (S2a) in the three-body E_{K_f} data (Figure 1 in the main text), confirms that this channel is negligibly if at all populated.

1.3 Internal energy in the products

In the main text, we assign the main feature in the two-body data to production of $NO(X) + NO_2(\tilde{C})$, with a deposited internal energy consistent with the relevant FCFs. To show this, we have calculated the FCFs between the cation ground state, $NO^+(X)$, and the neutral ground state, NO(X), and these are plotted in Figure S3a. The results indicate that a vertical electron capture process with $\Delta v = 0$ ($v = 0 \rightarrow 0$) does not have the largest FCF, and that $\Delta v = 1, 2$ ($v = 0 \rightarrow 1, 2$) have a larger vibrational overlap with the ion ground state, yielding an expected average vibrational energy of 0.7 eV in the ground state neutral NO product. For the FCFs between NO_2^- and NO_2, we are guided by the results of Weaver *et al.* [31]. Figure S3b shows the photoelectron kinetic energy spectrum, recast here as internal energy in the neutral NO_2. Assuming

only the $NO_2(\tilde{C})$ state is populated in our experiment, the average internal energy, including electronic excitation energy,for this state is 2.3 eV. Combining this analysis yields an average energy of ≈3 eV deposited into the NO and NO_2 neutral molecules, which would mean that they share ≈4 eV of kinetic energy, i.e., as is observed in the E_{K_f} spectrum in the main manuscript.

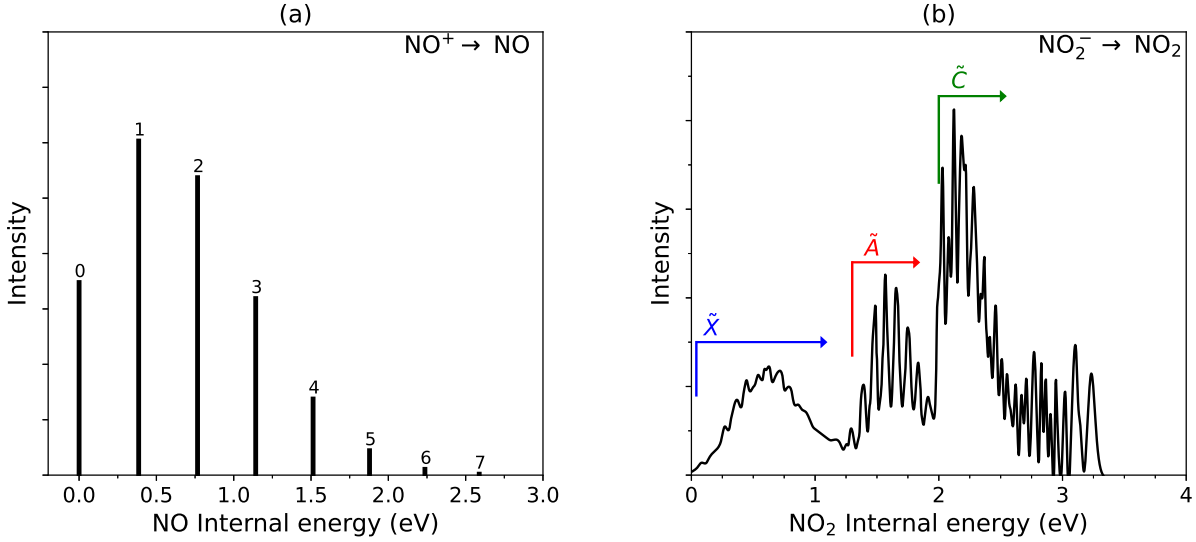

Fig. S3 Expected internal energy distribution in the NO/NO_2 products, based on: a. calculated Franck-Condon factors for the $NO^+(X)$ and NO(X) potentials; b. the experimental photoelectron spectrum from photodetachment of cold NO_2^- at 213 nm (5.825 eV), adapted from [31]

1.4 Electronically excited states in NO_2 and wave-packet propagation on these states

Vertical transitions dominate efficient e^--capture by the cation [1], requiring an equally favourable vertical detachment process in the molecular anion. The extra electron in $NO_2^-(\tilde{X}\ ^1A_1)$ creates a non-bonding electron pair, exerting a greater repulsion on the O atoms, such that, while retaining C_{2v}-symmetry, the O-N-O angle is considerably reduced from 134° to ≈118°, and the bond-length is increased slightly from $r_{NO} \approx 120$ pm to $r_{NO} \approx 125$ pm. Calculations and florescence spectroscopy

[39, 41, 51] indicate that the $\tilde{C}$ state minimum has C_s symmetry with unequal N-O bonds: $r_{NO^1} \approx 148$ pm and $r_{NO^2} \approx 111$ pm.

We have performed quantum dynamics calculations to explore the dissociation dynamics and associated lifetimes for wavepackets representing cold NO_2^- following vertical excitation onto the lowest 4 neutral surfaces. This is illustrated in Figure 3 in the main text where a grey bar indicates the equilibrium anion geometry projected onto the states of the neutral. In the figure, some *ab initio* data is plotted for two additional higher states since they complete the block of six states that dissociate to the NO(X $^2\Pi_r$) + O(^{3}P) asymptote. The two higher states are shown for reference, but weren't fitted into surfaces as part of an earlier study [41] and were therefore excluded from the dynamics calculations described next.

To generate the initial wavepacket for the cold anion, a near-equilibrium ground state anion PES was constructed via a harmonic expansion at the CCSD(T)-F12b/VTZ-F12 level. The Multi-Configurational Time-Dependent Hartree (MCTDH) method was used to converge the lowest zero-point vibrational level found at 0.213 eV (1716.6 cm^{-1}). Next, the wavepacket was separately promoted onto each of the neutral electronic states, centred at the positions highlighted by the grey bar in Figure 3 in the main text. Each wavepacket was then propagated on the coupled manifold of fitted electronic states using the MCTDH method. The wavepackets are free to explore energetically accessible regions of the PES and due to the couplings between PESs may also split into different components on the various surfaces. Each surface also extends to describe dissociation to the NO(X $^2\Pi_r$) + O(^{3}P) ground state products asymptote, via symmetry equivalent extension of either N-O bond. In the calculations a complex absorbing potential (CAP) was employed beginning at r_{NO}=265 pm (5.0 a_0) to absorb any flux of the wavepacket reaching dissociation, and

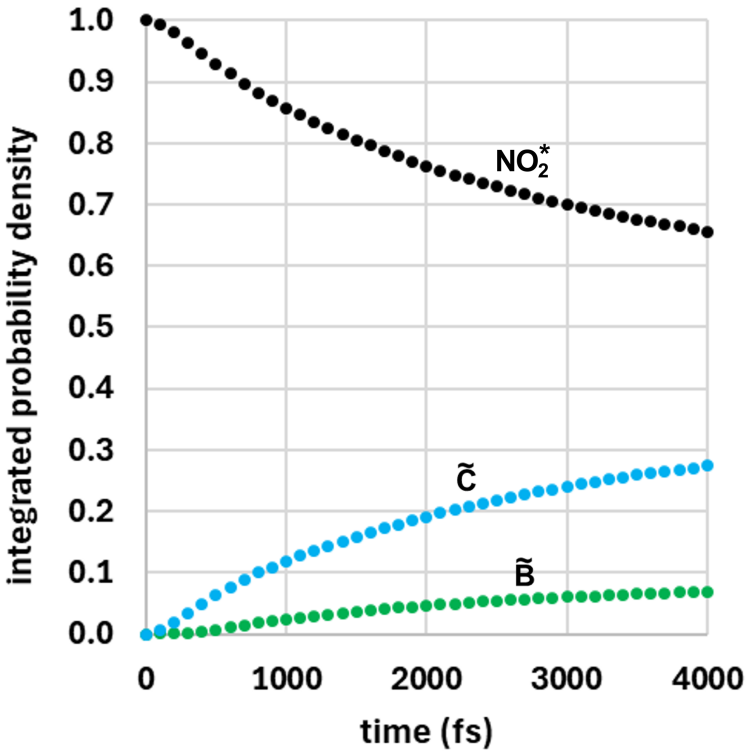

Fig. S4 The undissociated population of the wavepacket is plotted (in black) as a function of propagation time, shown here following initial vertical excitation to the NO_2 $\tilde{B}$ state. The portion of the wavepacket reaching dissociation on the $\tilde{B}$ state is recorded separately from the (larger) portion that dissociates after crossing onto the $\tilde{C}$ state (see text).

the fraction of the wavepacket absorbed at the boundary on each state was recorded as a function of the propagation time.

Figure S4 shows an example of the decaying wavepacket population for the NO_2 $\tilde{B}$ state which corresponds to a fitted lifetime of 12.5 picoseconds. Table S1 lists the computed lifetimes for each of the lowest four states. Note that in measurements of NO_2's absorption spectrum [52], photodissociation was observed to turn on near the absorption maximum, around 25,000 cm^{-1} (3.10 eV). That is 3.10 eV above the zero-point energy, or 3.33 eV above the minimum on the PES. Thus for wavepackets starting in the Franck–Condon region, as seen in Table S1, only the $\tilde{B}$ state at 3.8 eV

on the neutral PESs (as well as the higher "$\tilde{E}$" and "$\tilde{D}$" states) is expected to have sufficient energy to dissociate. The two energies listed in Table S1 for each electronic state are that of the Franck–Condon point for that state, relative to the minimum on the ground $\tilde{X}$ state of the neutral, and for convenience also relative to the zero-point-energy of the anion (where the experiment begins). Indeed, not surprisingly, the NO_2 $\tilde{X}$ and $\tilde{A}$ states, which at the anion geometry are located only 0.52 and 1.74 eV above the minimum respectively, and so no dissociative flux was recorded at the asymptote. The wavepacket on the $\tilde{C}$ state PES is met with a gradient in the asymmetric stretch direction, which is essentially the dissociation coordinate, however with an energy of 2.27 eV it too lacks sufficient energy to dissociate and is also stable indefinitely from a dynamical standpoint. The $\tilde{B}$ state wavepacket at 3.8 eV does have sufficient energy to dissociate. Interestingly, as shown in Figure S4 most of the dissociation for the $\tilde{B}$ state wavepacket occurs after crossing onto the $\tilde{C}$ state. Beginning at the Franck–Condon point on the $\tilde{B}$ state, the wavepacket follows the gradient towards its linear minimum, but as shown in Figure S4, first crosses the $\tilde{C}$ state. The portion that crosses onto the $\tilde{C}$ state from the $\tilde{B}$ state has much more energy than any wavepacket reaching the $\tilde{C}$ state by vertical excitation from the anion. Thus, as seen in Figure S4, following an induction period during which the wavepacket crosses onto the $\tilde{C}$ state, and follows its gradient in the asymmetric stretch direction, it quickly finds its way to the dissociation asymptote. In contrast, the portion that stays on the $\tilde{B}$ state past the crossing point, tends to oscillate in the bending coordinate, and thus is significantly slower to find the dissociation channel. The total undissociated population, depleted by both mechanisms, was fit to a lifetime for the $\tilde{B}$ state wavepacket of 12.5 picoseconds.

Table S1 Electronic energy levels, energies, state symmetries, and lifetimes against dissociation, for the six lowest lying states in neutral NO_2 at the anion or neutral ground state (gs) geometry.

			Order with respect to symmetry			Energy with respect to		Lifetime against dissociation
	$^2A'$	$^2A''$	$^2A'$	$^2A''$	NO_2^- gs geometry	NO_2 gs (eV)	NO_2^- gs (eV)	(ps)
$\tilde{X}$	$^2A_1$		1^{st}		1^{st}	0.52	≈2.56	∞
$\tilde{A}$	$^2B_2$		2^{nd}		2^{nd}	1.74	≈3.78	∞
$\tilde{B}$		$^2B_1$		1^{st}	4^{th}	3.80	≈5.84	12.5
$\tilde{C}$		$^2A_2$		2^{nd}	3^{rd}	2.27	≈4.31	∞
"$\tilde{D}$"	(3A′)		3^{rd}		6^{th}	≈5.45	≈7.49	N/A
"$\tilde{E}$"		(3A″)		3^{rd}	5^{th}	≈4.70	≈6.74	N/A

1.5 Comparison to Flowing Afterglow measurements

Prior studies of mutual neutralization of NO^+ with various anions in a flowing afterglow, either by Smith and co-workers [13, 14] (NO_2^-, I^-, Cl^-) or Tsuji et al. [15, 45–47] (SF_6^-, $C_6F_6^-$, $C_6F_5^-$, $C_6F_5Cl^-$, $C_6F_5Br^-$, $C_6F_5CF_3^-$) have reported production of $NO(A^2\Sigma^+)$ via observation of the radiative emission to the ground state. For reactions with several of these anions (I^-, SF_6^-) production of the slightly higher energy $NO(B^2\Pi_r)$ state or ($C_6F_6^-$, $C_6F_5^-$, $C_6F_5Cl^-$, $C_6F_5Br^-$, $C_6F_5CF_3^-$) substantially higher energy $NO(C^2\Pi_r)$ and NO ($D^2\Sigma^+$) states are also reported. Both experimental designs are sensitive only to product states emitting between 200 - 700 nm (Tsuji et al.) or 200 - 600 nm (Smith and co-workers). Because there are product channels to which the afterglow experiments are completely blind, the observed products could account for essentially any fraction from being very minor to 100%. Tsuji et al. do not address this point, nor does Smith and co-workers for the $NO^+ + NO_2^-$ reaction. However, Smith and co-workers do interpret similar results for the $NO^+ + I^-$ and $NO^+ + Cl^-$ reactions that an estimate of the photon volume emission rate in the experiment implies that $NO(A^2\Sigma^+)$ is formed in a "substantial fraction" of recombination events, at odds with the present results.

Historically, measurements of dissociative recombination in flowing afterglows and in storage rings have had quantitative differences, with somewhat modest success in

resolving those discrepancies. The results here could also differ due to the differing nature of the experiments. The flowing afterglow and storage ring experiments occur in distinct pressure regimes. Products formed in the storage ring will not undergo further collisions prior to detection, whereas in the flowing afterglow (at ≈1 Torr) products will collide with the helium buffer gas at a frequency of 10^6 s^{-1}. However, reducing the collisional frequency should increase, not decrease the survival of excited state products, as would be needed to reconcile the results. Initial formation of more highly excited states that are preferentially stabilized by collisions to $NO(A^2\Sigma^+)$ also fails as an explanation as the radiative lifetime of $NO(A^2\Sigma^+)$ is too short. We are unable to identify a reasonable mechanism by which the flowing afterglow experiment can produce a much larger fraction of $NO(A^2\Sigma^+)$ than does the storage ring. As the FA experiment only is sensitive to reaction channels where NO is electronically excited while the storage ring measurements are sensitive to all reaction channels, the conclusion is, based on our present experimental results alone, that the FA experiment only was sensitive to a very minor component of the MN-process.

The three lowest vibrational states of $NO(A^2\Sigma^+)$ state radiatively decay to the ground state with a lifetime of about 200 ns.[53] The hard-sphere collision rate with the helium buffer gas at the stated pressure of 0.35 Torr is the same order of magnitude such that even in the strong-collision limit (i.e. quenching on every collision), a minimum of about one half of $NO(A^2\Sigma^+)$ will decay radiatively. At the stated flow velocity (10^2 m s^{-1}), decay will occur promptly on the timescale of the flowing afterglow experiment. The photon production rate per volume is then equal to the $NO(A^2\Sigma^+)$ product formation rate per volume:

$$[NO(A^2\Sigma^+)] = f_{NO(A)}[NO^+][X^-]k_\alpha, \tag{S3}$$

where k_α is the MN rate constant, reported as $6{\times}10^{-8}$ cm^3 s^{-1} at room temperature, and $f_{NO(A)}$ is the product branching fraction to NO($A^2\Sigma^+$). The ambipolar nature of the plasma dictates that $[NO^+] = [NO_2^-]$. At the lowest reported plasma densities of $5{\times}10^8$ cm^{-3}, the production rate is initially on the order of 10^{10} cm^{-3} s^{-1} and decreasing along the flow tube. The photon collection rate depends on detection sensitivity and geometric factors. Assuming an 8 cm diameter flow tube with a window centred 25 cm downstream of the ion source the solid angle for photon acceptance on a detector with an effective diameter, d, centred on the window can be calculated for any point in the flow tube. By convoluting this factor along with the decaying plasma density along the flow tube (assuming the reported k_α along with a typical ambipolar diffusion rate constant of 150 s^{-1}) and integrating over the volume, the expected photon collection rate, arbitrarily assuming a value of $d = 1$ cm, is approximately $f_{NO(A)} \approx 1{\times}10^9$ photons s^{-1}. This number may be reduced by up to a factor of 2 in the strong collision limit and by an additional order of magnitude for inefficiency in the detection itself, i.e., $f_{NO(A)} \approx 5{\times}10^7$ photons s^{-1}. This value will scale approximately as d^2, such that assumption of just a 1 mm detector effective diameter suggests $f_{NO(A)} \approx 1{\times}10^6$ photons s^{-1}. Interpretation of Figure 1 from reference[13] suggests collection of $\sim 5{\times}10^4$ photons s^{-1} from MN of $NO^+ + NO_2^-$ under the above conditions. As the assumptions here regarding photon collection are as pessimistic as we found justifiable, we approximate an upper limit on $f_{NO(A)}$ of about 0.05 in line with the present data.